Antibiotics-induced conformational heterogeneity of a multidrug transporter revealed by single-molecule FRET

Hassan Maklad[1*], Tom Kache[2*], Aurélie Roth[1], Maria Mamkaeva[1], Cédric Govaerts[1°], Jelle Hendrix[2°] and Chloé Martens[1°]

[1]Biochemistry and Structural Biology, Université libre de Bruxelles (ULB), Boulevard du Triomphe, Building BC, B-1050 Brussels, Belgium

[2]Dynamic Bioimaging Lab, Advanced Optical Microscopy Centre and Biomedical Research Institute, Hasselt University, Agoralaan C (BIOMED), B3590 Diepenbeek

*co-first authors

°co-corresponding authors

Abstract

The rapid increase of bacterial multidrug resistance (MDR) is an urgent threat to human health. MDR transporters are membrane proteins that can transport a wide array of structurally dissimilar compounds and contribute to drug resistance by exporting different antibiotics from the cell. Whether such transporters exhibit common or distinct transport mechanisms for different substrates is poorly understood. In this work, we measured the time-resolved conformational dynamics of the model MDR transporter LmrP in its apo and ligand-bound state with single-molecule Förster resonance energy transfer (smFRET). We used multi-parameter Hidden Markov Modeling (mpH2MM) to characterize the underlying conformational states of LmrP in the presence of different antibiotics and to quantify their sub-millisecond interconversion kinetics. We observed substrate-dependent heterogeneity in the conformational landscape, both in terms of accessible states an conversion rates between them, suggesting that MFS MDR transporters can export structurally dissimilar antibiotics by relying on an array of underlying conformational states with substrate-dictated interconversion rates. This work provides novel insights into the mechanism of MDR transporters and advocates for combined structure/dynamics-based drug design when targeting their function.

Introduction

Multidrug resistance in pathogenic microorganisms presents a serious global threat (Catalano et al., 2022). It has been estimated that multidrug-resistant infectious diseases claim more than 2 million lives and cost around $170 billion annually (Burki, 2018). One strategy evolved by bacteria to resist antibiotics is the active extrusion of drugs across the cell membrane via transport proteins, thereby reducing the cytosolic concentration and efficacy of the drugs. This low-level resistance enables bacteria to survive and eventually acquire additional resistance mechanisms, such as target mutation or enzymatic degradation. A molecular-level understanding of the transport mechanism of efflux pumps is a prerequisite for the development of targeted inhibition strategies to re-sensitize resistant strains (Chitsaz & Brown, 2017). How a transport protein characterized by a specific structural fold can recognize and translocate substrates with widely differing chemical properties such as charge, size, and shape remains a fascinating enigma, and at the same time complicates the rational design of efflux pump inhibitors. Structural adaptation to chemically diverse substrates is observed for the prototypical efflux pump AcrB, which features distinct binding pockets and multiple substrate pathways. AcrB and its homologs, which belong to the same structural family of Resistance-Nodulation-Division (RND) transporters, play a prominent role in the emergence of multidrug-resistant phenotypes in Gram-negative bacteria (Du et al., 2014; Wang et al., 2017). These tripartite pumps are absent in Gram-positive bacteria, where most efflux systems belong to the Major Facilitator Superfamily (MFS). The molecular architecture of MFS efflux pumps differs markedly from that of RND pumps. MFS transporters, which represent the largest family of membrane transporters and are found across all domains of life, are composed of 12 to 14 transmembrane helical segments arranged in two bundles of six helices that surround a central binding pocket (Chitsaz & Brown, 2017; Quistgaard et al., 2016; Ranaweera et al., 2015). In bacteria, MFS efflux pumps can expel a broad range of cytotoxic molecules, including antibiotics, thereby conferring resistance to the bacterial cell (Blair et al., 2015; Du et al., 2018; Munita & Arias, 2016; Nikaido, 2009; Peterson & Kaur, 2018). MFS proteins mediate transport via the alternating access model, in which the transporter undergoes large conformational changes, alternating between inward- and outward-facing states that expose the central binding site to opposite sides of the membrane (Jardetzky, 1966).Reconciling the broad substrate promiscuity typical of multidrug efflux

pumps with the canonical architecture of MFS proteins opens up fundamental questions regarding active transport, specifically whether different antibiotics rely on independent transport pathways enabled by a shared structural scaffold.

In this study, we focus on the multidrug transporter LmrP from *Lactococcus lactis* bacteria. LmrP is a substrate/proton antiporter from the Major Facilitator Superfamily that can export several lipophilic molecules including antibiotics, fluorescent dyes, and detergents (Roth & Govaerts, 2018). We have previously investigated the coupling of LmrP conformational changes to protons and substrate binding using Double Electron-Electron Resonance (DEER) distance measurements on paramagnetically labelled protein mutants (Masureel et al., 2014; Martens et al., 2016; Claxton et al., 2015). These studies have shown that LmrP alternates between at least two conformational states, an inward-open (IO) and an outward-open (OO) state, in a protonation-dependent manner, where the protonation states of key acidic residues, specifically Asp68 and Glu327 orchestrate the transition (Masureel et al., 2014). The acidic residue Asp68, the most conserved in the MFS family, acts as the main conformational switch, as shown by a conservative mutation that stabilizes the inward-open conformation and abrogates transport (Masureel et al., 2014). In parallel, X-ray crystallography provided a high-resolution whole-protein structural view in the substrate-bound outward-open conformation (Debruycker et al., 2020). The structural information obtained via crystallography and DEER is obtained on fixed protein samples, where only the most stable conformations can be captured, leaving out a range of dynamically interconverting structural states composing the conformational landscape of the transport cycle (Mazal & Haran, 2019; Schuler & Hofmann, 2013). The observation and quantification of protein dynamic transitions between different structural states is a key to understanding the transport cycle at a molecular level.

Practically, this requires the identification of pathways between different structural states/conformations occupied for different time periods. Consequently, to provide a comprehensive image of the coupling between conformational changes, proton translocation, substrate binding, and transport, it is crucial to access time-correlated dynamics by identifying all transient states and extracting the underlying kinetics between them (Husada et al., 2018). Such insights are particularly relevant for multidrug transporters, where it is an open question whether the efflux

pump undergoes the same conformational transitions for different substrates, or whether distinct transport pathways exist within the same pump, allowing it to accommodate transport of structurally different substrates.

Single-molecule Förster resonance energy transfer (smFRET) is a powerful and versatile tool that provides molecular and mechanistic insights into biomolecules at the single-molecule level in solution and under physiologically relevant conditions (ambient temperature, physiological buffer, and low molar concentration)(de Boer et al., 2019). It is attracting more interest in investigating membrane transporters dynamics (Bartels et al., 2021; Gregorio et al., 2017; Krainer et al., 2019; Maslov et al., 2023). In FRET, a non-radiative energy transfer occurs from a donor fluorophore (D) to an acceptor fluorophore (A), where both are attached to specific sites on a protein molecule (Bartels et al., 2021; Husada et al., 2018). The efficiency of energy transfer *E* is highly sensitive to the distance between the donor and acceptor on the nanometer length scale (Fig. 1A)(Sasmal et al., 2016). Real-time tracking of *E* for single molecules in turn allows monitoring protein conformational changes and dynamics at nanometric spatial resolution combined with a wide range of accessible timescales (ns-minutes), thus complementing the ensemble biochemical and structural methods such as Nuclear Magnetic Resonance (NMR), X-ray crystallography, Electron Paramagnetic Resonance (EPR), and Cryogenic electron microscopy (Bartels et al., 2021; Ciftci et al., 2020). In this study, we employed the PIE-smFRET technique (multi-parameter fluorescence detection with pulsed-interleaved excitation) (Kudryavtsev et al., 2012) (Fig.1A) to study the conformational dynamics of LmrP and characterize its substrate-dependent conformational landscape. Our work reveals a complex interplay between ligand binding, conformational dynamics, and substrate translocation by LmrP, and showcase how both structural (different states) and kinetic (different rates between these states) heterogeneity supports the active transport of different antibiotics, while at the same time hinting at differences in transport rates are correlated with specific pathways within the conformational landscape.

Results

SmFRET charts the conformational landscape of LmrP

To track the real-time conformational changes of LmrP by smFRET, we selected specific sites located at the termini of transmembrane helices to attach a pair of FRET fluorophores. We replaced the selected residues with cysteines to enable the specific reaction with the reactive maleimide moieties of ATTO 488 and Alexa Fluor 647 fluorescent dyes. One extracellular (H98C-M374C) and one intracellular (K9C-K404C) distance reporter were selected to probe distance fluctuations on the opposing sides of the membrane transporter between the N- and C-terminal halves (Fig.1B). These sites are predicted to provide maximal conformational freedom for the attached dyes and ensure that structural changes between inward-open and outward-open conformations would result in clear FRET efficiency changes. We estimated the expected FRET efficiencies *E* based on the crystal structure in the outward-open conformation and the AlphaFold model in the inward-open conformation (Del Alamo et al., 2021). Their values, together with the corresponding expected distances between the probes in both conformations, are given in Table S.1. All double cysteine mutants were functionally tested by following LmrP-mediated transport of a known model substrate, Hoechst 33342, in *L. lactis* inverted membrane vesicles (Fig. S1A). Single-molecule FRET measurements were performed on the labeled LmrP molecules in detergent micelles, diluted to ~50-pM concentration, and freely diffusing through the femtolitre-size probe volume of the confocal microscope (Fig. 1A). The distribution of FRET efficiencies for all measured molecules is plotted as burst-wise *E* histograms. At pH7, the conformational landscape of apo-LmrP is characterized by a broad distribution of *E* on the extracellular side, with a maximum around *E* ≈0.5(Fig. 1C, left, blue histogram). On the intracellular side, the histogram displays a main central state with a maximum around *E* ≈0.5 (Fig. 1C, right, blue histogram). By comparing the observed to expected *E* values(Table S.1), we can conclude that the apo-protein at pH 7 adopts a flexible conformation that is predominantly closed on the intracellular side, while sampling states with different opening magnitudes on the extracellular side, with the state of intermediate opening being the most populated. This represents an outward-occluded/ inward closed conformation.

The reversible protonation of key acidic residues drives the conformational switch of the transporter (Masureel et al., 2014); thus, changes in pH modulate the conformational equilibrium

adopted by LmrP. Based on this, we assessed the effect of pH change on its conformational landscape using smFRET. At pH 5, on the extracellular side, we observe a shift in the distribution towards a population with $E \approx 0.8$, indicating closure upon lowering the pH (Fig. 1C, left, orange histogram). We observe one main population with $E \approx 0.3$ at the intracellular side, indicating a distance increase between probes and opening, compared to the apo protein at pH 7 (Fig. 1C, right,orange histogram). These observations are per our previous DEER measurements of LmrP, which showed that the protein changes its conformation in response to pH change (Masureel et al., 2014; Martens et al, 2016). We confirmed this observation with smFRET measurements by the extracellular reporter coupled with the D68N mutation, which is known to stabilize LmrP in the outward-closed/ inward-open state. At pH 7 and 5, the high-FRET states were more populated for the mutant, confirming that it corresponds to the assigned conformation (Fig. S2), and is not responding to pH change. Together, these experiments validate the ability of smFRET to identify and distinguish different conformational states of LmrP. Importantly, smFRET analyses up to this point report on burst-averaged values of *E*. If, however, the molecules interconvert rapidly between two (or more) FRET states while they diffuse through the probe volume, these states have an averaged histogram rather than distinct peaks as in the case of static populations (Santoso et al., 2010; Tsukanov et al., 2013)Therefore, in the following, we zoom in on the bursts to investigate the kinetic connectivity of different putative structural states of LmrP.

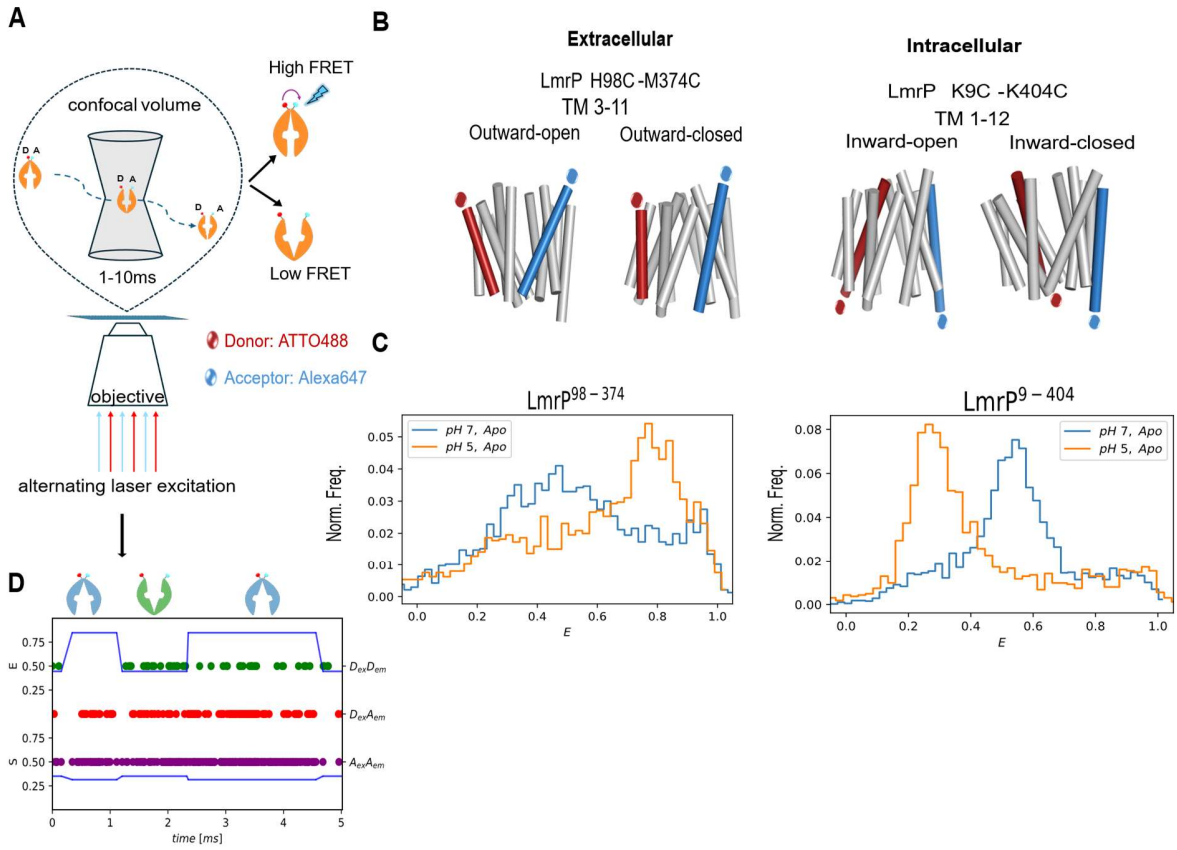

Figure 1. **smFRET charts the conformational landscape of LmrP**. **A**. Schematic illustration of the PIE smFRET experiment setup, showing the free diffusion of labelled LmrP molecules across the focal spot of an inverted fluorescence microscope. “D” and “A” correspond to donor and acceptor dyes, respectively. In the PIE setup, two spatially overlapped and alternatingly pulsing lasers are shooting at the objective to excite donor and acceptor fluorescence consecutively. Fluorescence signals of the donor and acceptor are recorded separately, and the fluorescence lifetime and anisotropy of each dye are determined.**B.**Cartoon representation of LmrP helices with 98C (TM3)-374C (TM11) in outward-open(OO) or outward-closed(OC) conformations, and LmrP 9C (TM1)-404C(TM12) in inward-open(IO) or inward-closed(IC) conformations. The fluorophores ATTO488 (red) and Alexa647 (blue), are represented by colored balls. The N- and C-halves are composed of TM1-6 and TM7-12, respectively. **C.** histograms of burst-wise FRET efficiencies displaying smFRET signatures of intra- and extracellular reporter mutants reveal conformational changes of LmrP upon pH change. **D.** A sample photon time trace of a single burst, with photons represented as colored dots, with donor excitation photons colored green and red for donor and acceptor, respectively. Acceptor excitation photons are colored purple. *E* (top panel) and *S* (bottom panel) of states determined from dwells.The most likely state path predicted by the Viterbi algorithm is overlayed as a blue horizontal line. Consecutive photons with the same state are considered as a single dwell, *E* and S values are then estimated as mentioned in (Harris *et al*., 2022).

Kinetic analysis of apo LmrP reveals transient hidden states

To characterize the conformational states underlying the burst-averaged FRET histograms and the time scales at which these states interconvert, the data were submitted to the multi-parameter photon-by-photon hidden Markov modeling (mpH^{2}MM) methodology to analyze smFRET trajectories(Harris et al., 2022; Kudryavtsev et al., 2012; Pirchi et al., 2016). In brief, this maximum likelihood modeling is based on the HMM machinery, which incorporates the donor and acceptor photon streams, without binning into fluorescence intensity time traces. mpH2MM analyzes smFRET data on the level of single photon time-trace of individual bursts (Fig. 1D) (Harris et al., 2022). It can extract the number of states involved in the underlying FRET dynamics within a single burst, their mean *E* values, the stoichiometry *S*, and the kinetic rate constants that dictate how long molecules typically dwell in a particular state (see Methods). The estimated mean dwell time extracted from the analysis is the time the molecule stays on average in a particular state, e.g. X, before transitioning to Y. We here annotated the states according to their mean *E* values as follows: state L (*E*≈0.1-0.4), state M (*E*≈0.4-0.7), and state H (*E*≈0.7-1). A subscript E or I is added when describing the FRET states on the extracellular or intracellular side

At pH 7, a three-state model was the best fit to describe the apo-state data from the distance reporters on either side of the membrane (Figure 2A). We observe that the interconversion kinetics between these states favor the intermediate FRET states M on both sides of membrane, where the protein dwells for longer before transitioning to the L or H FRET states, in which it resides only for about ~3ms on average. The noticeable difference between both sides is that the dwell time for the M state is ~4.7 ms on the extracellular side but extends for 11 ms on the intracellular side. The average conformation lifetime (sum of dwell times/number of states) for the apo-state at pH7 is 4.5ms. We use this average as an indicator for the global protein dynamics, which estimates the average time required for the protein to change its current conformational state. The mean *E* value of the predominant M state is ≈0.59 on the extracellular side and ≈0.54 on the intracellular side. At pH 5, as protonation of acidic residues involved in the conformational equilibrium occurs, the conformational landscape is modified, and a two-state model on both sides of the protein now best describes the data(Figure 2B). On the extracellular side, it displays an interconversion between FRET state L_E and FRET state H_E, with mean dwell times of ~3 ms and ~5 ms, respectively. On the intracellular side, the protein

mainly dwells for about ~15 ms in the FRET state L_I and shortly transitions to the FRET state H_I for ~4 ms. The observed mismatch in dwell times for the same state between extracellular and intracellular sides at both pHs suggests an intrinsic flexibility of individual transmembrane helices translated by differential occupancy of FRET states on each side of the transporter. Based on the alternating access model, the structural readout of the analysis suggests that at pH 7, LmrP-apo favors the previously mentioned outward-occluded conformation (Fig. 1B), while briefly sampling two other states: outward-open and inward-open conformations. While at pH5, the protonation induces mainly an outward-closed/inward-open conformation(Latorraca et al., 2017). Furthermore, protonation at pH5 induced slower dynamics, represented by a longer average dwell time of 6.9ms compared to 4.7ms for the apo-state.

LmrP displays distinct substrate-dependent conformational dynamics

To study ligand-modulated LmrP conformational dynamics, we performed smFRET measurements at a 2-mM saturating concentration of antibiotics from different classes, at pH 7, followed by mpH^2MM analyses. Four classes of antibiotics were tested: lincosamides (clindamycin), macrolides (roxithromycin), aminoglycosides (kanamycin), and β-lactams (ampicillin).

Qualitatively, in the presence of clindamycin, the burst-averaged *E* histogram peak of the extracellular reporter shifted slightly towards a higher *E* value, while the histogram peak of the intracellular reporter moved slightly towards a lower *E* value compared to the apo state (Fig.3A, blue histogram). This indicates a structural rearrangement upon binding. The *E* histogram distributions in the presence of ampicillin and kanamycin showed no noticeable difference compared to the apo state (Fig. 3B and D, blue histogram).

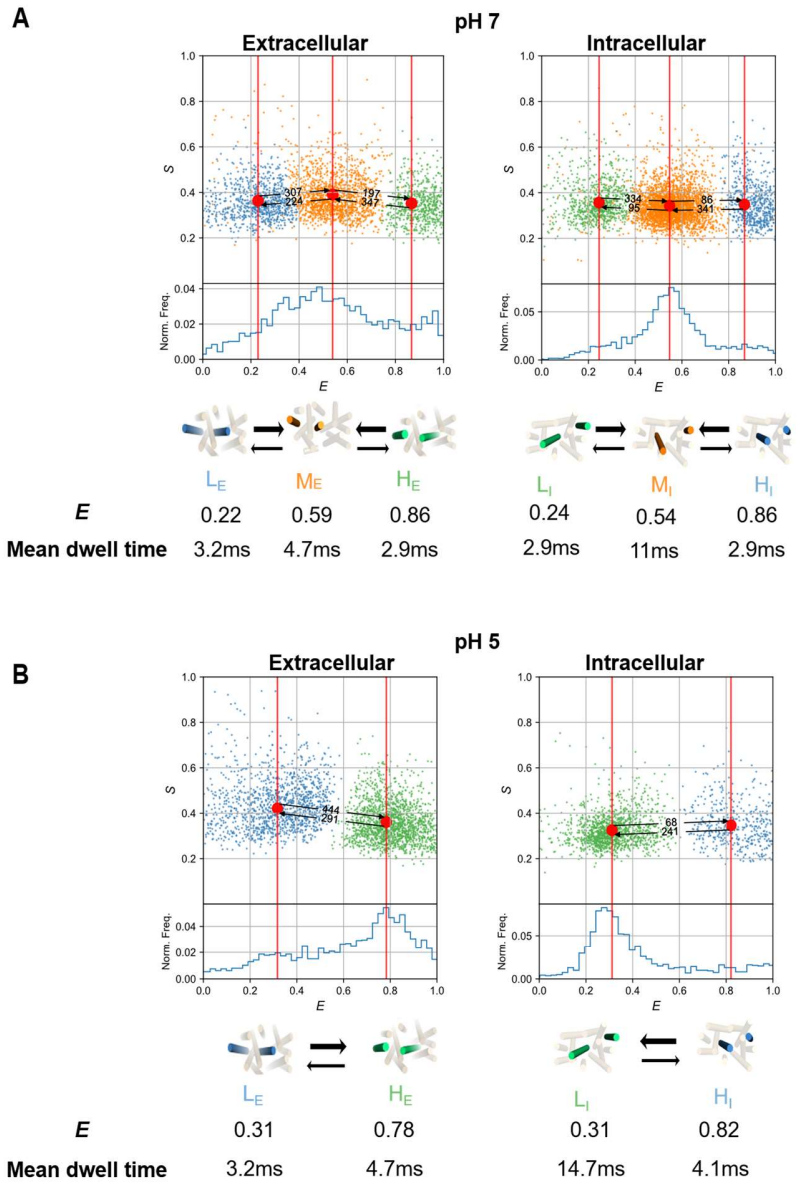

Figure 2. **Kinetic analysis of apo LmrP reveals transient hidden states. A.**The plots of data analysis of LmrP apo-state at pH 7. Upper panel :On top the E-S scatter plot of the corrected dwells. Dwells are colored based on the assigned state of the chosen mpH2MM model. Red circles represent the mean *E* value of each state, and the numbers above the arrows represent the transition rate constants (s^{-1}) between the two FRET states. At the bottom: Burst-wise FRET histogram showing the post-purified corrected bursts. Lower panel: Cartoon representations of the adopted confirmation for interconverting FRET states. The *E* value and mean dwell time in ms for each state are mentioned below. The extracellular distance reporter data are on the left, and the intracellular distance reporter data are on the right **B.**The plots of data analysis of LmrP at pH 5. Same organization as in **A**.

In contrast, the burst-averaged *E* histogram obtained upon addition of macrolide roxithromycin clearly resembles that observed at pH 5, indicating stabilization of an outward-closed/inward-open conformation (Fig. 3C, blue histogram). This is evident from a highly populated high FRET state of E≈0.8 on the extracellular side, and a main FRET state of *E*≈0.36 on the intracellular side, referring to closing on the extracellular side and opening towards the cytosol.

Next, quantitative kinetic state analysis was done via mpH^{2}MM. For clindamycin, a three-state model on the extracellular side and a two-state model on the intracellular side are the most likely fit for the data. The extracellular distance reporter showed no noticeable difference compared to the apo state (Figure 3A).On the intracellular side, the protein resided for a dwell time of 3ms in state M_I with *E*≈0.45, and for 1.1ms in state H_I with a mean *E*≈0.8. The average conformation lifetime with clindamycin is 4ms, compared to 4.5ms for the apo-state, indicating a relatively accelerated dynamics. It is noteworthy that the clindamycin-induced M_I state has a lower *E* value compared to its corresponding M_I of the apo-state (*E*≈ 0.54), suggesting a conformational state that is relatively more open on the intracellular side.

With kanamycin, a two-state model was predicted on the extracellular side and a three-state model on the intracellular side (Fig. 3B). On the extracellular side, the protein dwells for 2.4 ms in state H_E with mean *E*≈0.75 before transition to state L_E with mean *E*≈0.37, where it dwells for 3.2 ms. On the intracellular side, it dwells in state M_I with mean *E*≈0.58 for 6ms before transitioning to state H_I or L_I for 2ms. Kanamycin induces faster dynamics than the apo-state at pH7, with an average conformation lifetime of 3.1 ms.The interconversion rates between states on both sides are thus considerably faster, and the M_E state is not stabilized.

For roxithromycin, the mp^{2}HMM analyses predicted a two-state model for the extracellular reporter data, and a three-state model on the intracellular side(Fig. 3C). Extracellularly, the protein interconverts between the state L_E with mean *E*≈0.34 and the state H_E with mean *E*≈0.78. The transition rates between the two states lead to a mean dwell time of 3.6 ms in state L_E and 5.7 ms in state H_E, respectively. Hence, the H_E state is relatively more populated. On the intracellular side, the conformational equilibrium is shifted towards the FRET state L_I of *E*≈0.27, for a mean dwell time of 12ms. Consequently, this state is more populated, compared to the briefly visited states M_I of *E*≈0.55 and H_I of *E*≈0.87, with mean dwell times of 3ms and 4.3ms, respectively. The average conformation lifetime with roxithromycin is 5.8 ms , indicating that its binding

induces a specific response, with slower dynamics than the apo-state, clindamycin and kanamycin, and stabilizes an outward-open/inward-closed conformation.

With ampicillin, the most likely models were a two-state model on the extracellular side, and a three-state model on the intracellular side (Fig. 3D). The extracellular distance reporter data shows interconversion between the low FRET state L_E with mean E≈0.36 and the high FRET state H_E with mean E≈0.85, with mean dwell time of 3ms and 2ms, respectively. The two states are thus relatively similarly populated. On the intracellular side, a three-state model is predicted. The conformational equilibrium is shifted towards the intermediate FRET state M_E of E≈0.55, for a mean dwell time of 13ms. This represents slightly slower dynamics than that of the apo state at pH7, with an average conformation lifetime of 4.7ms. Measurements were performed with 2mM glucose, a hydrophilic substrate that is not a ligand of LmrP, as a control. A three-state model was identified as the best fit on both sides of the membrane, with a conformational dynamics and kinetic profile resembling that of the apo-state (Fig.S.3), indicating that it is probably not binding to LmrP.

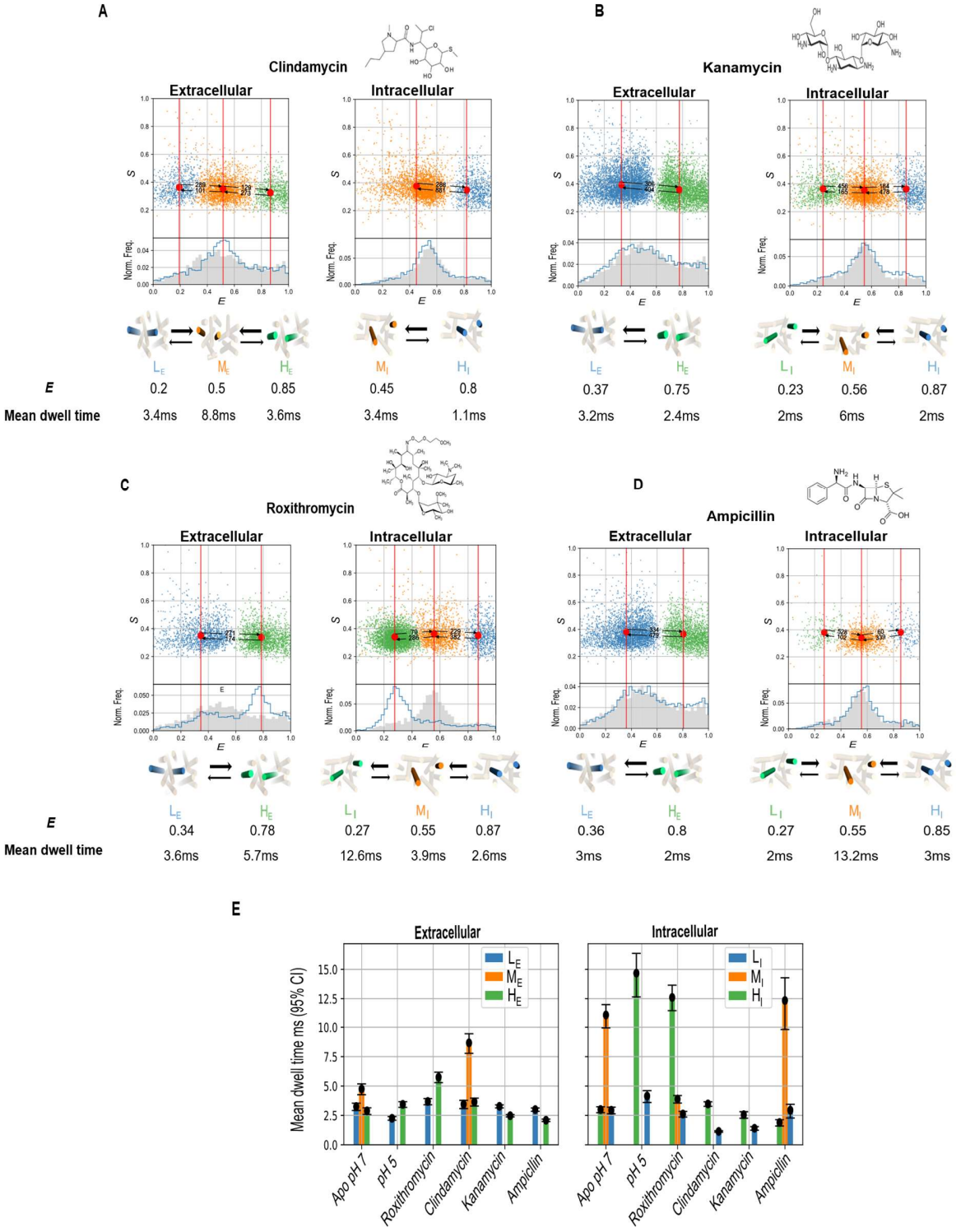

Figure 3. **LmrP displays distinct substrate-dependent conformational dynamics. A-D** The plots of data analysis of LmrP with different antibiotics. Upper panel: On the top the E-S scatter plot of the corrected dwells. Dwells are colored on the basis of the assigned state of the chosen mpH2MM model. Red circles represent the average

E value of each state, and the numbers above the arrows represent the transition rate constants (s^{-1}) between the two FRET states. At the bottom: Burst-wise FRET histogram showing the post-purified corrected bursts. Lower panel: Cartoon representations of the helices movement showing the adopted confirmation of the interconverting FRET states. The mean *E* value and mean dwell time in ms for each state are mentioned below. The extracellular distance reporter data on the left, and the intracellular distance reporter data are on the right **E.** Bar chart showing the mean dwell times in ms of different FRET states with different antibiotics for the distance reporters on the extracellular side and the intracellular side.The error bars represent the upper and lower limits of 95% confidence interval.

Different kinetic profiles have different resistance profiles

We speculated that these differences between the substrates induced conformational dynamics could translate into a difference in transport efficiency, that would impact resistance. To test this, we monitored the cell growth of *L.lactis NZ9000* strain transformed with *lmrp*-containing plasmid under the control of a nisin-inducible promoter, in which the multidrug transporters LmrA and LmrCD are deleted. Putman et al., 2000; Venter et al., 2008) The assays were done for LmrP wild-type (WT) and the transport-deficient mutant D68N, to compare the relative efficiency of antibiotic efflux as a function of cell survival at different drug concentrations. The minimum inhibitory concentration MIC of each tested antibiotic was calculated (Kowalska-Krochmal & Dudek-Wicher, 2021). MIC is the least concentration required to inhibit the bacterial growth. It indicates the relative ability of cells to survive the presence of the antibiotic assayed; the higher the MIC relative to the mutant, the more tolerant the cells to the antibiotic, suggesting more efficient LmrP efflux activity. In the presence of clindamycin (Fig. 4.A), we observed an approximately 40 times increase in the minimum inhibitory concentration required to inhibit the growth of cells expressing the LmrP WT relative to the D68N mutant. For kanamycin, we observed an 80 times increase of MIC for the WT, indicating a clear influence of LmrP mediated transport (Fig. 4B). The MIC difference for roxithromycin dropped to less than 2 folds. With ampicillin, the MIC ratio of WT to mutant strain was close to 1, implying that ampicillin is not transported by LmrP (Fig.4C-D). The differences in cell survival with structurally different antibiotics imply that LmrP efflux activity is substrate-specific. We then compared difference in survival with the kinetic profiles of each antibiotic that we obtained.

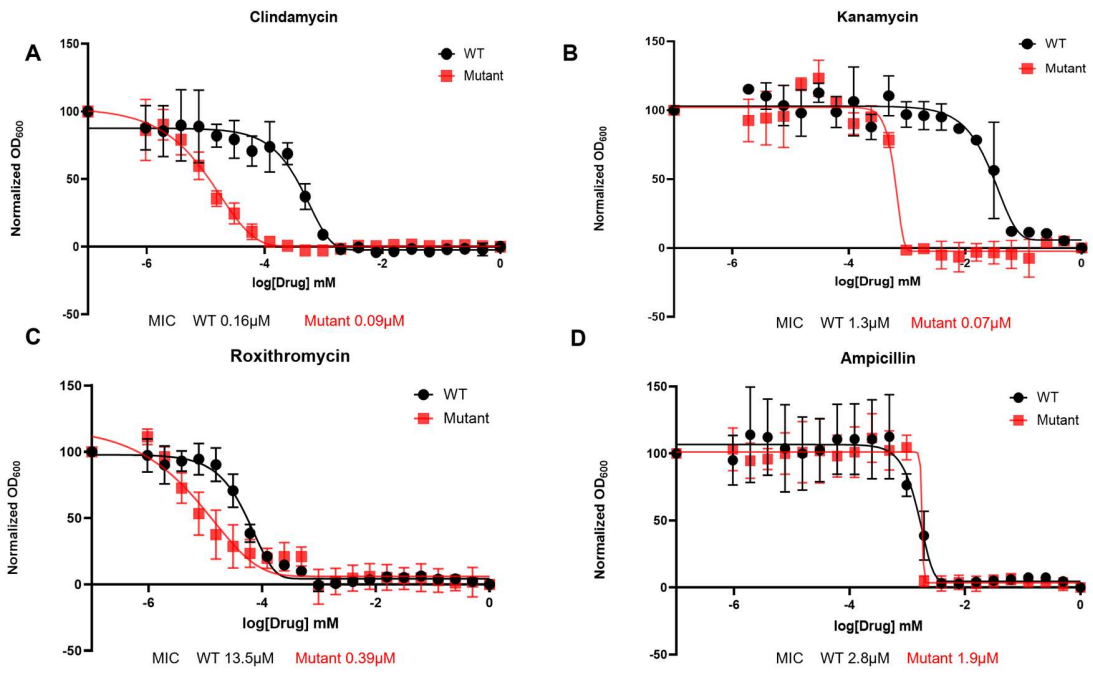

Figure 4.**LmrP mediated antibiotic resistance.** Cell growth assays of *L. lactis* expressing LmrP wild-type (WT, black), and transport-deficient D68N (mutant, red) in the presence of clindamycin(A), ampicillin (B) , roxithromycin (C) and kanamycin (d). The minimum inhibitory concentration MIC in μM of each antibiotic, for each strain is shown below each plot. Data in A-D show means and SD for n = 8 replica. MIC values with limits of 95% CI are shown in table S.2.

Discussion

In this study, we used smFRET to investigate how the conformational dynamics of the MFS MDR transporter LmrP is affected by binding of different antibiotics. The main finding of this work is that LmrP shows substrate-dependent conformational dynamics.

Using smFRET we were able to probe the distance changes between the labels on helices termini, reflecting the structural rearrangements between the two lobes of LmrP on both sides of the membrane. The analysis of FRET efficiency histograms showed how LmrP displayed the conserved elements of alternating access in detergent micelles: the inward-open and outward-open conformations. We clearly observe how initiating protonation by changing the pH from 7 to 5 shifted the histograms peaks from low to high FRET states and vice versa, depicting the conformational switch from outward open to inward open states. This agrees with what was previously described about LmrP protonation driven conformational switch((Masureel et al., 2014) , and proved the functionality of our LmrP-FRET setup. As a multidrug transporter, LmrP

is expected to be more flexible in order to sample different transport-competent conformations to fit a wide range of chemically and structurally dissimilar substrates (Yardeni et al., 2020). To further unravel hidden interconverting conformational states we took advantage of the PIE-smFRET setup, where every single photon arrival time and detection channel is recorded, providing a time correlated donor and acceptor photon streams. We analyzed our FRET data via the multiparameter hidden Markov modeling (mpH^{2}MM) to elucidate the number of interconverting states and quantify their transition rates in different conditions. Our analysis revealed that LmrP apo state at pH7 oscillates between three different states, as probed by distance reporters on both membrane sides. It mainly resides in an outwar-occluden/inward-closed conformation characterized by intermediate *E* values and also briefly visits two other states characterized by either lower or higher *E* values, while never directly converting from low to high FRET states and vice versa. At pH5, LmrP oscillates between two different *E* states , maintaining an outward-closed/inward-open conformation, while the main populated intermediate FRET state at pH7 is not observed. This points to large scale conformational dynamics induced by protonationcompared to the range of conformations assumed by the apo-state.

Furthermore, LmrP shows substrate-dependent conformational dynamicsWe performed the smFRET measurements tested the presence of different antibiotics. The mpH^{2}MM analyses revealed ligand-dependent conformational landscape.

It has been suggested that LmrP transporter works by “hydrophobic vacuum cleaner” model (Roth & Govaerts, 2018), meaning that it binds its lipophilic ligands from the inner leaflet of the membrane before being transferred to the central binding pocket on their way to the extracellular milieu. Hence, the initial contacts between the ligand and the transporter occurs at the intracellular side. The conformational landscape and resolve dynamics on the intracellular side is thus of considerable interest in understanding the ligand-specific response. It is noteworthy that clindamycin and roxithromycin are lipophilic with CX logP of 1.04 and 3 respectively(ChEMBL) while kanamycin and ampicillin are extremely hydrophilic with CX logP of -7.6 and -2.0 respectively. Interestingly, the two lipophilic substrates are the ones that induced conformational landscape on the intracellular side which is different from the apo-state. For clindamycin, the protein interconverts between two states M_I and H_I , while roxithromycin mainly stabilizes the L_I state, which is inward-open conformation. On the other hand, the conformational landscape induced by hydrophilic kanamycin and ampicillin resemble the three state

model of the apo-state. This indicates that the hydrophilic ligands might be binding directly from the cytoplasm, and so not diverting from the apo-state conformational distribution on the intracellular side. Moreover, with all antibiotics tested, the conformational landscape on the intracellular side always included the M_I and the H_I states To evaluate the LmrP-mediated transport *in* vivo we performed cell survival assays in presence of different antibiotics. The assays clearly point to differential LmrP-mediated survival ability. Clindamycin and kanamycin showed 40 and 80 times increase in the MIC values for the WT compared to the transport deficient mutant, while roxithromycin didn't reach a 2 fold increase.

Based on the alternating access model and the readout of our analysis, a swift transition from the occluded conformation (M_I) to outward-open conformations (H_I) is crucial for successful transport. This is obvious in case of clindamycin and kanamycin, which are both efficiently transported (given the cell survival assays) which induce accelerated transitions between these states relative to the apo-state at pH7. This is indicated by the mean dwell time in M_I for 3.4 ms and 6 ms for clindamycin and kanamycin respectively, compared to 11 ms for the apo-state. On the other hand, ampicillin is stuck in the M_I state for 13ms (11ms for apo) while roxithromycin is stuck in state L_I for 12 ms, indicating that the transition to outward conformation is severely impeded. The dynamics data and the growth assays point to a plausible link between conformational dynamics speed and the transport efficiency of LmrP. Our results also show that apo-LmrP assumes different conformational states which enables binding of wide array of structurally and chemically dissimilar molecules. It also show how the transport efficiency is dictated by the transition kinetics between key conformers. This work provides deeper insights into molecular mechanisms of multidrug transporters and shed light on their hidden aspects of their promiscuity.

Materials and Methods

Bacterial strains, plasmids and growth conditions

LmrP was expressed in the *L. lactis* NZ9000 strain that is deleted of the known ABC multidrug transporters LmrA and LmrCD(Putman et al., 2000; Venter et al., 2008). We used the in-home pHLP5 plasmid, a derivative of the *L. lactis* expression vector pNZ8048 carrying the lmrP gene coding for the C-terminally 6 Histidine-tagged LmrP(Putman et al., 1999). Briefly, cells were

grown at 30 °C in M17 broth supplemented with 0.5% (w/v) glucose and 5 µg/mL chloramphenicol until the OD660 reaches 0.7. The overexpression of LmrP was then induced by the addition of 1:1000 dilution of the supernatant of the nisin-producing *L. lactis* strain NZ9700(Kuipers et al., 1993; Mierau & Kleerebezem, 2005). After 2h of induction at 30 °C, cells were harvested by centrifugation at 7000 ×g.

Design and construction of the mutants

For each distance reporter, two residues were selected to be mutated into cysteines based on the structure of LmrP obtained by X-ray crystallography in the outward-open conformation (PDB 601Z) as well as on the model of the inward-open conformation obtained by inverted-topology repeats by our collaborator José D. Faraldo-Gómez. Cysteines were placed at the extracellular and intracellular extremities of chosen TMs while avoiding mutating conserved residues. The expected FRET efficiencies were estimated by simulating the fluorescent probes' accessible volume using FRET Positioning and Screening software (FPS) (Kalinin et al., 2012) so that they are separated by a distance within the Förster radius, 56.8 Å in this case. The accessible volume (AV) clouds were simulated using the parameters given for ATTO488 and Alexa647 in (Vandenberk et al., 2018).

The plasmid template was first methylated using the dam methyltransferase (NEB), following the manufacturer's recommendations and as described in(Monk et al., 2010) Mutations were introduced by site-directed mutagenesis using the Pfu DNA polymerase (Promega) in the in-home pHLP5 plasmid, in which an alanine had previously replaced the only endogenous Cys270. The primers were designed as described in(Liu & Naismith, 2008). After transformation, plasmid DNA was extracted and verified by sequencing.

Preparation of inside-out membrane vesicles

As previously described(Putman et al., 1999) ,cells were washed in 50 mM HEPES pH 7. They were resuspended (10 mL for each L of culture) in the same buffer supplemented with 7 mg/mL of lysozyme from chicken egg whites, 10µg/mL Deoxyribonuclease I from bovine pancreas, 10 mM $MgSO_4$, and 50mM Dithiothreitol (DTT). After 90min incubation at 30 °C, cells were homogenized with a Potter-Elvehjem-type tissue grinder and lysed by four passes at 1000–1500 bars using a high-pressure homogenizer. Cell debris and undisrupted cells were subsequently

eliminated by centrifugation at 17,000 × g. Inside-out membrane vesicles were then isolated by ultracentrifugation of the supernatant at 100,000 ×g for 2h at 4°C. Membranes were resuspended in a pH7 buffer of 100 mM HEPES, 300 mM NaCl, 20% (w/v) glycerol (5 mL buffer/L culture) and 1mM DTT.

Transport assays

The transport activity of LmrP mutants was assessed by measuring Hoechst fluorescence (EX 355 nm, EM 457 nm) decay over time at 30°C, based on previously published protocols (Putman et al., 1999; Putman et al., 2000; (Masureel et al., 2014).Briefly, inside-out membrane vesicles of LmrP-expressing cells (~1mg proteins) were diluted in transport buffer (50 mM HEPES, 2mM MgCl2, 300 mM KCl, pH 7.4) with 0.3µM of Hoechst (Invitrogen). The addition of 3 mM of ATP-Na2 in 50 mM HEPES pH 6.8 buffer supplemented with 250 mM MgSO4 allows the generation of a proton gradient by activating the endogenous F0F1-ATPase. Active extrusion of Hoechst by LmrP is detected by a decrease of fluorescence. Addition of 1µM of the ionophore nigericin dismisses the proton gradient and Hoechst is no longer actively extruded by LmrP, causing the fluorescence to increase. Raw data were normalized for fluorescence intensities relative to the initial fluorescence prior to ATP addition.

LmrP purification and labelling for smFRET

Inside-out membrane vesicles were solubilized in a solution of 2.5% (w/V) n-dodecyl- β – D-maltoside (β-DDM) in water with 1 mM DTT. After 1.5 h incubation on a rotating wheel at 4 °C, the insoluble part was removed by ultracentrifugation at 100 000 × g for 1 h. The supernatant was batch-incubated with Ni^{2+}-nitrilotriacetate affinity resin (Ni-NTA; Qiagen; 500 µL resin/L of culture) with 10mM imidazole at 4°C for 2h. The resin was pre-equilibrated with buffer A (50mM HEPES, 150mM NaCl, 10% (w/V) glycerol, 20mM imidazole, and 0.05% (w/V) β-DDM, pH 7). After the incubation, the slurry was transferred into a polypropylene column, the flow-through discarded, and the resin was washed with 8 CV of buffer A, supplemented with 0,5mM DTT. LmrP was then eluted by stepwise additions of buffer B (buffer A with 250mM imidazole and 0,5mM DTT). The more concentrated fractions were pooled together. Imidazole and DTT were removed just prior to labelling using a desalting column (Disposable PD10 desalting columns, GE Healthcare) previously equilibrated with labelling buffer (50mM HEPES, 150mM NaCl and 0.02% (w/V) β-DDM, pH 7.5) that was degassed in vacuum/N2 under continuous stirring. LmrP

was concentrated to approximately 100µM using a 50kDa MWCO concentrator (Amicon, GE Healthcare) and then labelled with the donor ATTO488 (ATTO 488 maleimide, ATTO-TEC GmbH) and the acceptor Alexa647 (Alexa Fluor 647 maleimide, Life Technologies Europe BV). 250µM Alexa647 and 100µM ATTO488 were mixed in the degassed Labelling buffer and 50µM of LmrP was added for 2h at RT. Unreacted dye was removed on a desalting column, and the labelled protein was run on an SDX-200 10/300 GL (GE Healthcare) size exclusion chromatography column in SEC buffer (50 mM HEPES, pH 7, 150 mM NaCl, 10% (w/v) glycerol, and 0.02% (w/v) β-DDM). The efficiency of the labelling was checked via UV-visible absorbance at 280nm, 501nm, and 650nm to estimate the amount of LmrP, ATTO488, and Alexa647, respectively, after correcting the 280nm peak for the dyes' absorbance.

Confocal Multiparameter-PIE Microscope setup

The experimental measurements were recorded using a home-built multiparameter fluorescence confocal microscope operating with pulsed-interleaved excitation (Hendrix & Lamb, 2013; Kudryavtsev et al., 2012; Maslov et al., 2023).

Two pulsed lasers were used for excitation with excitation wavelengths of 483nm (LDH-P-C-470, Picoquant, Berlin, Germany) and 635nm (LDH-P-C-635B, Picoquant, Berlin, Germany) with clean-up filters for both excitation sources (Chroma ET485/20x, F49-482,AHF Analysentechnik, Tübingen, Germany and Chroma z635/10x, Picoquant, Berlin, Germany). Both lasers were operated with a pulse frequency of 26.67 MHz (PDL 828 "Sepia 2", Picoquant, Berlin, Germany)(and delayed by 18ns relative to each other. The laser beams were reflected using mirrors and dichroic mirrors into an optical fiber (60FC-4-RGBV11-47 and PMC-400Si-2.6-NA012-3-APC-150-P, Schäfter und Kirchhof, Hamburg, Germany). After the fiber, the beams were collimated (60FC-L-4-RGBV11-4 7, Schäfter und Kirchhoff, Hamburg, Germany), passed through a linear polarizer (Codixx VIS-600-BC-W01, F22-601, AHF, Tübingen, Germany) and reflected into the backport of a microscope body (X70, Olympus Belgium NV, Berchem, Belgium) using a 3mm thick excitation polychoric (zt 405/488/561/640tpc, AHF, Tübingen, Germany) and two mirrors. The power of the excitation sources was measured and adjusted to the desired power before the beam entered the microscopy body using a laser power meter. Excitation powers of 100µW and 50µW were set for the 483nm and 635nm excitation sources, respectively. The excitation lasers were focused into the sample volume using a water-immersion objective lens (UPLSAPO-60XW, Olympus), and the confocal spot was focused about

10µm into the measured solution. The emission was collected through the objective lens, transmitted through the polychroic mirror, focused through (AC254-200-A-ML, Thorlabs, Bergkirchen, Germany) a 75 µm-pinhole (P75S, Thorlabs), and collimated again (AC254-50-A-ML, Thorlabs). Subsequently, the emission was spectrally separated using dichroic mirrors. The 483-nm emission (referred to as B) is reflected (Chroma T560lpxr, F48-559, AHF), filtered (Chroma ET525/50m, F47-525, AHF). The 635-nm emission (R) was passed through and filtered (Chroma ET705/100m, AHF). Both emission beams are furthermore separated according to their polarization (BS252, Thorlabs) and then detected using four avalanche photodiodes, two for the parallel (∥) and perpendicular (⊥) polarization components of each spectral range (PD-100-CTE, MPD for B∥ and B⊥; EG&G SPCM-AQR12/14 for R∥ and R⊥). The detector outputs were routed (HRT-82, Becker & Hickl, Berlin, Germany) to and recorded with a TCSPC card (SPC-630, Becker & Hickl). The experimental TCSPC data were recorded in a 12-bit format encoding for the total experiment time ("macrotime"), time relative to the laser excitation pulse ("nanotime"), and a detector identification signal. Data processing of the recorded TCSPC data is discussed in the section Burstwise Data Processing((Kudryavtsev et al., 2012; Tomov et al., 2012)).

Single-Molecule FRET Data Recording

Before performing sample measurements, the alignment of the smFRET microscope was confirmed by measuring a mixture of 5 nM each of ATTO488-COOH and ATTO655-COOH in water. The setup was aligned to achieve brightnesses of > 100kHz for the donor and >70kHz for the acceptor detectors with laser excitation powers of 100 and 50 µW for the donor and acceptor excitation laser, respectively. The purified and double-labeled LmrP protein was diluted in measurement buffer: 50 mM HEPES pH 7 (adjusted for 20°C, Sigma-Aldrich), 150 mM NaCl (VWR Normapur), 0.02 % β-DDM (w/V, Carl Roth) to a concentration of approximately 50 pM and to achieve a burst event frequency of 10 to 20 / s. For measurements in the presence of a substrate, the burst concentration-diluted solution of protein was allowed to incubate with the indicated substrate concentration on ice for 30 minutes. The measurement buffer was recorded without the protein to confirm the absence of an excessive and potentially interfering signal contribution. This was repeated for each substrate with the same concentration as in measurements with labeled protein. The sample solution was recorded on an 8-well Nunc Lab-Tek chambered 1.0 cover glass (Thermo Fisher Scientific). The confocal observation volume was

focused about 10 µm above the surface of the cover glass into the sample solution. Measurements were recorded at room temperature (approximately 22 °C).

Burst-wise Data Processing

The experimentally recorded TCSPC data were processed by converting the recordings to the HDF5 format using the phconvert Python module (phconvert 2024). The data were further processed using the FRETbursts module(Ingargiola et al., 2016). The detector identification signals and detector timing ranges, which indicate the spectral range and polarization (the photon records of the two polariation channels per spectral channels were summed) of the detected photon, were assigned to either the donor excitation/donor emission ($D_{ex}D_{em}$), donor excitation/acceptor emission ($D_{ex}A_{em}$), or acceptor excitation/acceptor emission ($A_{ex}A_{em}$) to disentangle the recorded signal according to the pulsed-interleaved excitation scheme. The background contribution was estimated using a single-exponential fit with a 30-second time window and a background threshold of less than 1.7. Individual burst events were identified using an all-photon burst search with a 20-photon sliding window and a minimum burst event acceptance threshold of 7-times the background count rate. Burst-wise parameters, such as the burst-wise FRET efficiency *(E)* or stoichiometry *(S),* were automatically calculated by the FRETbursts module (see section Calculation of Burstwise Parameters and Parameter Correction)(Ingargiola et al., 2016). To remove bursts that only contained signal from either the donor or acceptor dye, a minimum of 60 DexDem or DexAem photons and at least 40 $A_{ex}A_{em}$ photons were required. The distribution of bursts in *E* and *S* was assessed for the presence of a FRET-active population with *S* of around 0.5 which indicates emissions from both the donor and acceptor dyes . .This removes bursts with predominantly non-emissive donor or acceptor dyes (with *S* of 1 and 0, respectively). The photon-count filtered set of bursts was loaded into the burst mpH^{2}MM module for removal of short-lives donor or acceptor blinking states using a four-state mpH^{2}MM fit. All photon streams ($D_{ex}D_{em}$, $D_{ex}A_{em}$, and $A_{ex}A_{em}$) were used for mpH^{2}MM fitting. The fit results were used to filter out individual burst events in which a molecule ever visited a non-FRET-active state during the transition time through the observation volume. This was achieved by identifying the states with near-1 and near-0 *S* and removing such burst events from the list of bursts. This procedure removed about half of the burst events from the presented data. A second round of mpH2MM analysis was performed with the cleaned dataset to describe

the dynamics of the data (see Hidden-Markov Model Fitting).(Harris et al., 2022; Ingargiola et al., 2016)

Calculation of Burst-wise Parameters and Parameter Correction

Using the pulsed interleaved excitation (PIE) scheme for smFRET, the FRET efficiency is defined as

$$E = \frac{I_{DA} - \alpha\, I_{AA} - \delta\, I_{DD}}{I_{DA} - \alpha\, I_{AA} - \delta\, I_{DD} + \gamma I_{DD}}$$

and the stoichiometry as

$$S = \frac{I_{DA} - \alpha\, I_{AA} - \delta\, I_{DD} + \gamma I_{DD}}{I_{DA} - \alpha\, I_{AA} - \delta\, I_{DD} + \gamma I_{DD} + I_{AA}}$$

Where I_{DA}, I_{AA} and I_{DD} are the background corrected number of photons detected in the acceptor detection channels after donor excitation, in the acceptor detection channels after acceptor excitation and in the donor detection channels after donor excitation, respectively; *α* is a correction factor for the direct excitation of the acceptor with the 483 nm laser; δ is a correction factor for the emission crosstalk of the donor in the acceptor channel and *γ* is a correction factor for the relative detection efficiency of the donor and acceptor (Kudryavtsev et al., 2012; Maslov et al., 2023).To account for instrument-specific difference of donor and acceptor signal detection efficiencies, the γ correction factor was determined by measuring a mixture of FRET-labeled DNA standards with two different FRET efficiencies and labeled with the same dyes as the LmrP protein (Alexa Fluor 488 and ATTO 647N) . The α and β correction values were determined from the protein measurements itself by fitting . The obtained *E-S* histogram was used to determine the corrections. The reader is referred to Maslov et al. for details on smFRET correction factors(Maslov et al., 2023; Tomov et al., 2012). The correction values were found to be similar between different measurement repeats. The following correction values were used for the processing of all presented datasets: α = 0.03, δ = 0.03, and γ = 1.2 .

Analysis of Intra-Bursts Dynamics with Hidden-Markov Model Fitting

The processed and blinking-removed set of bursts was used to assess each dataset for the presence of intra-burst dynamics.The processed and cleaned-up list of burst events (see section Burstwise Data Processing) were loaded into the burstH2MM module (Harris et al., 2022) to quantify and characterize states visited by the FRET-labeled samples. A multiparameter H^2MM fit was carried out (using the $D_{ex}D_{em}$, $D_{ex}A_{em}$, and $A_{ex}A_{em}$ photon streams) with a maximum of 3200 fit iterations to a maximum of five states. The integrated complete likelihood (ICL) criterion was assessed to predicted the most likely number of states in the model as described by Harris et al. (2022). The model with the lowest ICL value, or where the states had a mean stoichiometry of $S \approx 0.5$, corresponding to FRET active molecules exclusively, was selected for each condition. A model was rejected once the returned mean values for S were markedly different from what can be considered a FRET-active state. This is the case, for example, if an mpH^2MM model has split a states into two states with different *S* compared to the previous model with one state less. We rejected such models with a difference in *S* due to the fact that no meaningful conformational state can be inferred from such a model. We estimated the mean dwell time for each state from the extracted transition rate constants between states. The mean state dwell time was calculated as $tau_i = 1 / ((\sum k_i,j) / N_states)$ as the inverse sum of all exchange rates that depopulate state i divided by the number of depopulation paths. The burst classifications were used to visualize the distribution based on the total burst duration (burstwise histogram) or per-dwell basis (dwell-based scatter plot). The state-average FRET efficiency were used to compare different conditions. The uncertainty of the transition rates obtained by the best-fitting mpH^2MM model was tested with the log-likelihood ratio test which is implemented in the $burstH^2MM$ module. The 95%-confidence interval was calculated using the likelihood ratio test, where the log-likelihood was reduced by 1.92 from its optimal value to determine the bounds of the interval.

Cell survival assay

Mutant and WT LmrP genes were transformed into *L. lactis* strain NZ9000 ΔLmrA ΔLmrCD(Venter et al., 2008) through electroporation. Individual colonies were grown overnight and used to inoculate 10ml cultures of M17 (supplemented with 0.5% glucose, 5 µg/ml of chloramphenicol), which were then incubated statically at 30 °C until reaching an OD660 of ~0.7, when expression was induced through the addition of a 1:1,000 dilution of the supernatant of the nisin-producing *L. lactis* strain NZ900034(Kuipers et al., 1993). After 2 h of expression, cells

were diluted with M17 (supplemented with 0.5% glucose, 5 µg/ml of chloramphenicol and 1:1,000 dilution of the supernatant of the nisin-producing L. lactis strain NZ9000) to an OD660 of 0.05. These dilute solutions were then aliquoted into 96-well plates containing a dilution series of antibiotic within the M17 (supplemented with 0.5% glucose, 5 µg/ml chloramphenicol and a 1:1,000 dilution of the supernatant of the nisin-producing *L. lactis* strain NZ9000. The plates incubated to at 30 °C, without shaking, for 16 h before measuring the OD660 using Spark Multimode Microplate Reader(Tecan). The assays were conducted for at least three independent times, with eight replica for each antibiotic dilution per assay. After OD normalization, the data were fit to a Gompertz model to determine the MIC values (Lambert & Pearson, 2000)and corresponding standard error of the mean GraphPad Software Prism 10.3.

References

Bartels, K., Lasitza-Male, T., Hofmann, H., & Löw, C. (2021). Single-Molecule FRET of Membrane Transport Proteins. *Chembiochem : A European Journal of Chemical Biology*, *22*(17), 2657–2671.

Blair, J. M. A., Webber, M. A., Baylay, A. J., Ogbolu, D. O., & Piddock, L. J. V. (2015). Molecular mechanisms of antibiotic resistance. *Nature Reviews. Microbiology*, *13*(1), 42–51.

Burki, T. K. (2018). Superbugs: An Arms Race Against Bacteria. *The Lancet. Respiratory Medicine*, *6*(9), 668.

Catalano, A., Iacopetta, D., Ceramella, J., Scumaci, D., Giuzio, F., Saturnino, C., Aquaro, S., Rosano, C., & Sinicropi, M. S. (2022). Multidrug Resistance (MDR): A Widespread Phenomenon in Pharmacological Therapies. *Molecules (Basel, Switzerland)*, *27*(3). https://doi.org/10.3390/molecules27030616

Chitsaz, M., & Brown, M. H. (2017). The role played by drug efflux pumps in bacterial multidrug resistance. *Essays in Biochemistry*, *61*(1), 127–139.

Ciftci, D., Huysmans, G. H. M., Wang, X., He, C., Terry, D., Zhou, Z., Fitzgerald, G., Blanchard, S. C., & Boudker, O. (2020). Single-molecule transport kinetics of a glutamate transporter homolog shows static disorder. *Science Advances*, *6*(22), eaaz1949.

de Boer, M., Gouridis, G., Vietrov, R., Begg, S. L., Schuurman-Wolters, G. K., Husada, F.,

Eleftheriadis, N., Poolman, B., McDevitt, C. A., & Cordes, T. (2019). Conformational and dynamic plasticity in substrate-binding proteins underlies selective transport in ABC importers. *ELife*, *8*. https://doi.org/10.7554/eLife.44652

Debruycker, V., Hutchin, A., Masureel, M., Ficici, E., Martens, C., Legrand, P., Stein, R. A., Mchaourab, H. S., Faraldo-Gómez, J. D., Remaut, H., & Govaerts, C. (2020). An embedded lipid in the multidrug transporter LmrP suggests a mechanism for polyspecificity. *Nature Structural & Molecular Biology*, *27*(9), 829–835.

Del Alamo, D., Govaerts, C., & Mchaourab, H. S. (2021). AlphaFold2 predicts the inward-facing conformation of the multidrug transporter LmrP. *Proteins*, *89*(9), 1226–1228.

Du, D., Wang, Z., James, N. R., Voss, J. E., Klimont, E., Ohene-Agyei, T., Venter, H., Chiu, W., & Luisi, B. F. (2014). Structure of the AcrAB-TolC multidrug efflux pump. *Nature*, *509*(7501), 512–515.

Du, D., Wang-Kan, X., Neuberger, A., van Veen, H. W., Pos, K. M., Piddock, L. J. V., & Luisi, B. F. (2018). Multidrug efflux pumps: structure, function and regulation. *Nature Reviews. Microbiology*, *16*(9), 523–539.

Gregorio, G. G., Masureel, M., Hilger, D., Terry, D. S., Juette, M., Zhao, H., Zhou, Z., Perez-Aguilar, J. M., Hauge, M., Mathiasen, S., Javitch, J. A., Weinstein, H., Kobilka, B. K., & Blanchard, S. C. (2017). Single-molecule analysis of ligand efficacy in β2AR-G-protein activation. *Nature*, *547*(7661), 68–73.

Harris, P. D., Narducci, A., Gebhardt, C., Cordes, T., Weiss, S., & Lerner, E. (2022). Multi-parameter photon-by-photon hidden Markov modeling. *Nature Communications*, *13*(1), 1000.

Hendrix, J., & Lamb, D. C. (2013). Pulsed interleaved excitation: principles and applications. *Methods in Enzymology*, *518*, 205–243.

Husada, F., Bountra, K., Tassis, K., de Boer, M., Romano, M., Rebuffat, S., Beis, K., & Cordes, T. (2018). Conformational dynamics of the ABC transporter McjD seen by single-molecule FRET. *The EMBO Journal*, *37*(21). https://doi.org/10.15252/embj.2018100056

Ingargiola, A., Lerner, E., Chung, S., Weiss, S., & Michalet, X. (2016). FRETBursts: An Open Source Toolkit for Analysis of Freely-Diffusing Single-Molecule FRET. *PloS One*, *11*(8), e0160716.

Jardetzky, O. (1966). Simple allosteric model for membrane pumps. *Nature*, *211*(5052), 969–970.

Kalinin, S., Peulen, T., Sindbert, S., Rothwell, P. J., Berger, S., Restle, T., Goody, R. S., Gohlke, H., & Seidel, C. A. M. (2012). A toolkit and benchmark study for FRET-restrained high-precision structural modeling. *Nature Methods*, *9*(12), 1218–1225.

Kowalska-Krochmal, B., & Dudek-Wicher, R. (2021). The minimum inhibitory concentration of antibiotics: Methods, interpretation, clinical relevance. *Pathogens*, *10*(2), 165.

Krainer, G., Keller, S., & Schlierf, M. (2019). Structural dynamics of membrane-protein folding from single-molecule FRET. *Current Opinion in Structural Biology*, *58*, 124–137.

Kudryavtsev, V., Sikor, M., Kalinin, S., Mokranjac, D., Seidel, C. A. M., & Lamb, D. C. (2012). Combining MFD and PIE for accurate single-pair Förster resonance energy transfer measurements. *Chemphyschem : A European Journal of Chemical Physics and Physical Chemistry*, *13*(4), 1060–1078.

Kuipers, O. P., Beerthuyzen, M. M., Siezen, R. J., & De Vos, W. M. (1993). Characterization of the nisin gene cluster nisABTCIPR of Lactococcus lactis. Requirement of expression of the nisA and nisI genes for development of immunity. *European Journal of Biochemistry*, *216*(1), 281–291.

Lambert, R. J., & Pearson, J. (2000). Susceptibility testing: accurate and reproducible minimum inhibitory concentration (MIC) and non-inhibitory concentration (NIC) values. *Journal of Applied Microbiology*, *88*(5), 784–790.

Latorraca, N. R., Fastman, N. M., Venkatakrishnan, A. J., Frommer, W. B., Dror, R. O., & Feng, L. (2017). Mechanism of substrate translocation in an alternating access transporter. *Cell*, *169*(1), 96-107.e12.

Liu, H., & Naismith, J. H. (2008). An efficient one-step site-directed deletion, insertion, single and multiple-site plasmid mutagenesis protocol. *BMC Biotechnology*, *8*(1), 1–10.

Maslov, I., Volkov, O., Khorn, P., Orekhov, P., Gusach, A., Kuzmichev, P., Gerasimov, A., Luginina, A., Coucke, Q., Bogorodskiy, A., Gordeliy, V., Wanninger, S., Barth, A., Mishin, A., Hofkens, J., Cherezov, V., Gensch, T., Hendrix, J., & Borshchevskiy, V. (2023). Sub-millisecond conformational dynamics of the A adenosine receptor revealed by single-molecule FRET. *Communications Biology*, *6*(1), 362.

Masureel, M., Martens, C., Stein, R. A., Mishra, S., Ruysschaert, J.-M., Mchaourab, H. S., & Govaerts, C. (2014). Protonation drives the conformational switch in the multidrug transporter LmrP. *Nature Chemical Biology*, *10*(2), 149–155.

Mazal, H., & Haran, G. (2019). Single-molecule FRET methods to study the dynamics of proteins at work. *Current Opinion in Biomedical Engineering*, *12*, 8–17.

Mierau, I., & Kleerebezem, M. (2005). 10 years of the nisin-controlled gene expression system (NICE) in Lactococcus lactis. *Applied Microbiology and Biotechnology*, *68*(6), 705–717.

Monk, I. R., Casey, P. G., Hill, C., & Gahan, C. G. M. (2010). Directed evolution and targeted mutagenesis to murinize Listeria monocytogenes internalin A for enhanced infectivity in the murine oral infection model. *BMC Microbiology*, *10*, 318.

Munita, J. M., & Arias, C. A. (2016). Mechanisms of Antibiotic Resistance. *Microbiology Spectrum*, *4*(2). https://doi.org/10.1128/microbiolspec.VMBF-0016-2015

Nikaido, H. (2009). Multidrug resistance in bacteria. *Annual Review of Biochemistry*, *78*, 119–146.

Peterson, E., & Kaur, P. (2018). Antibiotic Resistance Mechanisms in Bacteria: Relationships Between Resistance Determinants of Antibiotic Producers, Environmental Bacteria, and Clinical Pathogens. *Frontiers in Microbiology*, *9*, 2928.

Pirchi, M., Tsukanov, R., Khamis, R., Tomov, T. E., Berger, Y., Khara, D. C., Volkov, H., Haran, G., & Nir, E. (2016). Photon-by-Photon Hidden Markov Model Analysis for Microsecond Single-Molecule FRET Kinetics. *The Journal of Physical Chemistry. B*, *120*(51), 13065–13075.

Putman, M., van Veen, H. W., & Konings, W. N. (2000). Molecular properties of bacterial multidrug transporters. *Microbiology and Molecular Biology Reviews: MMBR*, *64*(4), 672–693.

Putman, M., van Veen, H. W., Poolman, B., & Konings, W. N. (1999). Restrictive use of detergents in the functional reconstitution of the secondary multidrug transporter LmrP. *Biochemistry*, *38*(3), 1002–1008.

Quistgaard, E. M., Löw, C., Guettou, F., & Nordlund, P. (2016). Understanding transport by the major facilitator superfamily (MFS): structures pave the way. *Nature Reviews. Molecular Cell Biology*, *17*(2), 123–132.

Ranaweera, I., Shrestha, U., Ranjana, K. C., Kakarla, P., Willmon, T. M., Hernandez, A. J., Mukherjee, M. M., Barr, S. R., & Varela, M. F. (2015). Structural comparison of bacterial multidrug efflux pumps of the major facilitator superfamily. *Trends in Cell & Molecular Biology*, *10*, 131–140.

Roth, A., & Govaerts, C. (2018). LmrP from Lactoccoccus lactis: a tractable model to understand secondary multidrug transport in MFS. *Research in Microbiology*, *169*(7–8), 468–477.

Santoso, Y., Torella, J. P., & Kapanidis, A. N. (2010). Characterizing single-molecule FRET dynamics with probability distribution analysis. *Chemphyschem : A European Journal of Chemical Physics and Physical Chemistry*, *11*(10), 2209–2219.

Sasmal, D. K., Pulido, L. E., Kasal, S., & Huang, J. (2016). Single-molecule fluorescence resonance energy transfer in molecular biology. *Nanoscale*, *8*(48), 19928–19944.

Schuler, B., & Hofmann, H. (2013). Single-molecule spectroscopy of protein folding dynamics--expanding scope and timescales. *Current Opinion in Structural Biology*, *23*(1), 36–47.

Tomov, T. E., Tsukanov, R., Masoud, R., Liber, M., Plavner, N., & Nir, E. (2012). Disentangling subpopulations in single-molecule FRET and ALEX experiments with photon distribution analysis. *Biophysical Journal*, *102*(5), 1163–1173.

Tsukanov, R., Tomov, T. E., Berger, Y., Liber, M., & Nir, E. (2013). Conformational dynamics of DNA hairpins at millisecond resolution obtained from analysis of single-molecule FRET histograms. *The Journal of Physical Chemistry. B*, *117*(50), 16105–16109.

Vandenberk, N., Barth, A., Borrenberghs, D., Hofkens, J., & Hendrix, J. (2018). Evaluation of Blue and Far-Red Dye Pairs in Single-Molecule Förster Resonance Energy Transfer Experiments. *The Journal of Physical Chemistry B*. https://doi.org/10.1021/acs.jpcb.8b00108

Venter, H., Velamakanni, S., Balakrishnan, L., & van Veen, H. W. (2008). On the energy-dependence of Hoechst 33342 transport by the ABC transporter LmrA. *Biochemical Pharmacology*, *75*(4), 866–874.

Wang, Z., Fan, G., Hryc, C. F., Blaza, J. N., Serysheva, I. I., Schmid, M. F., Chiu, W., Luisi, B. F., & Du, D. (2017). An allosteric transport mechanism for the AcrAB-TolC multidrug efflux pump. *ELife*, *6*. https://doi.org/10.7554/eLife.24905

Yardeni, E. H., Mishra, S., Stein, R. A., Bibi, E., & Mchaourab, H. S. (2020). The multidrug transporter MdfA deviates from the canonical model of alternating access of MFS transporters. *Journal of Molecular Biology*, *432*(20), 5665–5680.